Geophysical Research Letters

Key Points:
- Before slip, gouge in reverse faults (load-strengthening path) compacts, whereas gouge in normal faults (load-weakening path) dilates
- The mean stress that the fault experiences before reactivation affects its compaction state, and thus its stiffness
- The stress path history of a fault influences its seismic behavior, especially in the presence of thick gouge-bearing fault zones

Correspondence to:

C. Giorgetti,
carolina.giorgetti@epfl.ch

The Influence of Loading Path on Fault Reactivation: A Laboratory Perspective

C. Giorgetti[1] and **M. Violay[1]**

[1]Laboratory of Experimental Rock Mechanics (LEMR), IIC-ENAC, École Polytechnique Fédérale de Lausanne (EPFL), Lausanne, Switzerland

Abstract The loading path the fault experiences is often neglected when evaluating its potential for reactivation and the related seismic risk. However, stress history affects fault zone compaction and dilation, and thus its mechanics. Therefore, in incohesive fault cores that could dilate or compact, the role of the loading path could not be ruled out. Here we reproduce in the laboratory different tectonic loading paths for reverse (load-strengthening in the absence of significant fluid pressure increase) and normal gouge-bearing faults (load-weakening) to investigate the loading path influence on fault reactivation and seismic potential. We find that, before reactivation, experimental reverse faults undergo *compaction*, whereas experimental normal faults experience *dilation*. Additionally, when reactivated at comparable normal stress, normal faults are more prone to slip seismically than reverse faults. We infer that the higher mean stress normal faults experience compacts more efficiently the fault rock, increasing its stiffness and favoring seismic slip.

Plain Language Summary Slip along pre-existing faults in the Earth's crust occurs whenever the shear stress resolved on the fault plane overcomes its frictional strength, potentially generating catastrophic earthquakes. The increase in the shear stress can follow different tectonic loading paths, and in particular, load-weakening versus. load-strengthening paths when it is coupled respectively to a decrease versus. an increase in the normal stress clamping the fault. The role of the loading path cannot be ruled out, especially in the presence of a thick, incohesive fault zone that can change its volume under different stress conditions. However, in most friction experiments, the fault is loaded under constant or increasing the normal stress, that is, load-strengthening. Here, we bridge the gap in laboratory loading paths simulating reactivation at the same normal stress clamping the fault but with different tectonic stress histories. Interestingly, our results suggest contrasting hydro-mechanical behavior for load-strengthening versus. load-weakening path: (1) before reactivation, fault zone compaction versus. dilation and (2) when reactivated at comparable normal stress, stable creep versus seismic slip, respectively. Our study has only scratched the surface of the loading-path influence on thick fault stability and potential implications for fluid circulation in fault zones, stressing the importance of further investigating the loading path influence.

1. Introduction

The occurrence of natural and induced slip along pre-existing faults have long been framed within the Mohr-Coulomb theoretical framework (e.g., Bolognesi & Bistacchi, 2016; Collettini & Trippetta, 2007; Gan & Elsworth, 2014; Jacquey et al., 2015; Jaeger, 1960; Leclère & Fabbri, 2013; Sibson, 1985; Williams et al., 2019). Accordingly, fault reactivation occurs whenever the resolved shear stress on the fault plane overcomes the fault frictional strength (e.g., Copley, 2017; Lisle & Srivastava, 2004; Morris et al., 1996). Based on the assumption of a planar, cohesion-less fault, this condition only depends on fault friction (μ), the angle between the fault plane and the maximum principal stress (θ), and the magnitude of the principal effective stresses (σ'_1, σ'_2, σ'_3). In this theoretical framework, the differential stress for fault reactivation $\sigma_D = \sigma_1 - \sigma_3$ is defined as follow (e.g., Sibson, 1985):

$$\sigma_D = \frac{1 + \mu \cot \theta}{1 - \mu \tan \theta} \sigma'_3 - \sigma'_3 \tag{1}$$
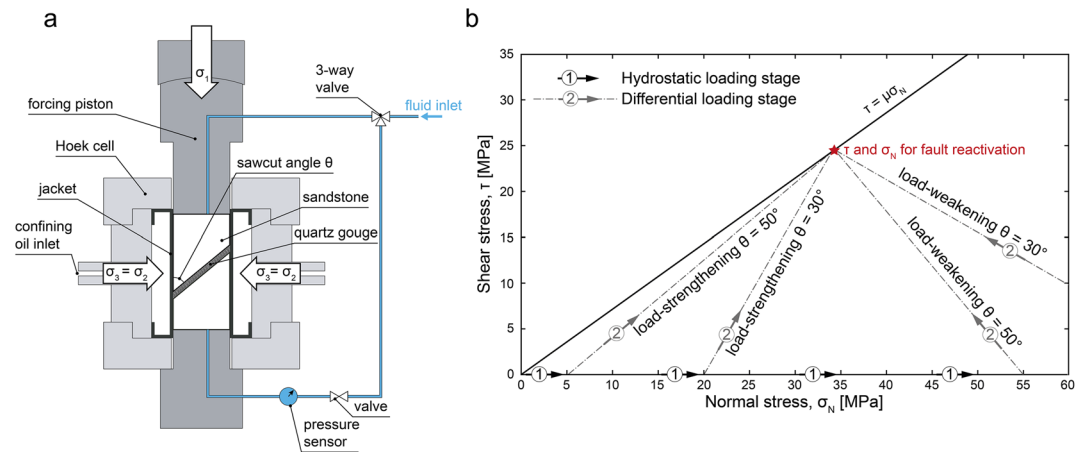
Figure 1. (a) Sketch of the experimental set-up: the forcing piston applies the vertical force to the cylindrical sample, the confining oil in the Hoek cell applies an isotropic lateral pressure, and a syringe pump applies pore fluid pressure. (b) Loading paths the samples underwent: stage 1 is the hydrostatic pressure increase, and stage 2 is the differential loading until reactivation occurs.

Although this simple approach is reliable, it does not consider the stress history of the fault experienced before the slip. Fault stress history can be described by the loading path, defined as the locus of the stress points representing successive stress states in shear stress (τ) versus normal stress (σ_N) plane (Figure 1b).

It is well known that different loading paths commonly occur in natural fault zones. They range from load-strengthening, when the increase in τ is coupled with an increase in σ_N, to load-weakening, when the increase in τ is coupled with a decrease in σ_N (Anderson, 1905; Sibson, 1993). Load-strengthening path (LSP) is commonly associated to reverse faults (in the absence of significant fluid pressure increase) and load-weakening path (LWP) to normal faults (Sibson, 1993). Recent studies (e.g., Petruccelli et al., 2019; Schorlemmer et al., 2005) show that the faulting type (normal, strike-slip, or reverse), and thus the loading path, influences the seismic behavior of faults. Nonetheless, the influence that the loading path possibly exerts on the mechanics of fault reactivation remains unclear. Particularly, the loading path could play a key role in the presence of thick, incohesive fault rocks. Incohesive gouge and pulverized rocks are often observed in shallow portions of faults (e.g., Agosta & Aydin, 2006; Ferraro et al., 2020). The clamping versus unclamping of the incohesive fault rock due to σ_N changes during loading could lead to *compaction* versus *dilation* of the fault zone, affecting its hydro-mechanical behavior.

Few previous studies have focused on compaction associated with LSP (e.g., Rutter & Glover, 2012), framing it within the critical state theory (e.g., Schofield & Wroth, 1968). Laboratory experiments to investigate fault mechanics are commonly conducted at constant σ_N (e.g., Di Toro et al., 2011; Dieterich, 1972; Marone, 1998) or imposing an LSP (e.g., Savage et al., 1996). Only a few experiments were conducted with an initial LWP before shearing at constant σ_N, just to reduce the displacement necessary to achieve the steady-state (e.g., Chester & Logan, 1990; Rutter & Maddock, 1992). Recently, focusing on fluid-injection in geo-reservoirs, LWPs have been imposed in laboratory faults increasing the pore fluid pressure (e.g., French et al., 2016; Noël et al., 2019; Passelègue et al., 2020, 2018; E. Rutter & Hackston, 2017; Scuderi et al., 2018).

A thorough understanding of the mechanics of fault reactivation is crucial to the assessment of fault activity (e.g., Worum et al., 2004), the related seismic hazard (e.g., Harris & Simpson, 1992; Sumy et al., 2014), and the seismic risk associated with geo-reservoir exploitation (e.g., Moeck et al., 2009). Here, taking advantage of a new laboratory approach specifically designed to investigate the influence of the loading path on the reactivation of gouge-bearing fault, we systematically document, for the first time, mechanical and hydrological differences between load-strengthening and load-weakening in gouge-bearing faults.

2. Materials and Methods

We performed triaxial saw-cut experiments with cylindrical samples of Rothbach sandstone (68% quartz, 16% feldspar, ∼12% clay, and 3% oxides and mica; e.g., Bésuelle et al., 2003) with saw-cut oriented at 30° and 50° to the sample axis and filled with quartz gouge (<125 μm in grain size; ∼6 and ∼4 g for, respectively, $\theta = 30°$ and $\theta = 50°$ to result in an initial ∼2-mm-thick layer). The experiments were carried out under room temperature and both nominally dry and water-saturated conditions. We conducted the experiments using a uniaxial press equipped with a Hoek cell to apply confining pressure and a syringe pump to apply pore fluid pressure, installed at LEMR of EPFL, in Switzerland (Figure 1a; e.g., Noël et al., 2019). To reproduce different tectonic loading paths, we alternatively increased the axial stress (σ_1) to simulate LSPs or decreased the confining pressure (σ_3), to simulate LWPs (Figure 1).

First, in dry experiments, the sample was hydrostatically loaded at a rate of 0.033 MPa/s to the target σ'_3 for LSPs and the target σ'_1 for LWPs (Figure 1b). In water-saturated experiments, the sample was saturated directly in the Hoek cell at low hydrostatic stresses (2–5 MPa), injecting de-ionized water at the bottom of the sample with the syringe pump and leaving the top of the sample open to the atmosphere until a flow through the sample was established. Then, the pore fluid pipes were isolated from the atmosphere, and pore fluid pressure (P_f) was increased to 1 MPa. To flush out air, we opened the topmost pipe to the atmosphere for few seconds every 20 min for few times (∼4), that is, until no more air was detected in the water flowing out from the topmost pipe. Afterward, hydrostatic and pore fluid pressures were contemporaneously increased at rates of 0.033 MPa/s to the target $\sigma'_3 = \sigma_3$-P_f for LSPs and the target $\sigma'_1 = \sigma_1$-P_f for LWPs. Once the initial effective hydrostatic pressure ($\sigma'_1 = \sigma'_3$; 2–20 MPa for LSPs and 20–55 MPa for LWPs) was achieved, we waited 30 min to allow for gouge compaction. Then, LSPs and LWPs were imposed on the sample, respectively increasing the σ'_1 and decreasing the σ'_3 (Figure 1b). The imposed loading/unloading rates $\delta\sigma'_1$/δt and $\delta\sigma'_3$/δt range between 0.0035 and 0.0100 MPa/s to achieve reactivation after a comparable amount of time following different loading paths (Table S1).

The starting hydrostatic pressure values were chosen in order to achieve reactivation at the same σ_N for faults undergoing different loading paths (Figure 1b; Table S1). The tested effective normal stresses at reactivation are $\sigma'_N = \sigma_N$-$P_f \approx$ 20–35 MPa (Table S1). In water-saturated experiments, P_f is maintained constant during the experiments in order to result in a pore fluid factor, equal to P_f/σ_3 in LSPs and to P_f/σ_1 in LWPs (e.g., Sibson, 1993), $\lambda = 0.3$. LSP and LWP follow on a τ-σ_N plane a straight line described by the following equations, respectively:

$$\tau = \frac{\sin(2\theta)}{1 - \cos(2\theta)}\left(\sigma'_N - \sigma'_3\right) \tag{2}$$

$$\tau = \frac{\sin(2\theta)}{1 + \cos(2\theta)}\left(\sigma'_1 + \sigma'_N\right) \tag{3}$$

where τ and σ'_N are the far-field stresses acting on the fault (Figure 1a).

The measured axial displacement (d_a) is corrected for the load-point stiffness, the axial strain is calculated as $\varepsilon = d_a/h$, where h is the height of the undeformed sample and the axial strain rate as $\dot{\varepsilon} = \delta\varepsilon/\delta$t.

At the end of the dry experiments, some samples were preserved in resin and polished thin sections were obtained parallel to the sense of shear in order to perform microstructural analysis.

3. Results

3.1. Dry Experiments

Figure 2 shows the mechanical data resulting from the deformation of dry faults oriented at 30° (well-oriented) and at 50° (misoriented) to σ'_1. The evolution of σ_D with ε is characterized by a strongly non-linear increase until a steady-state is achieved Figures (2a and 2b). Here, we define the onset of the steady-state as
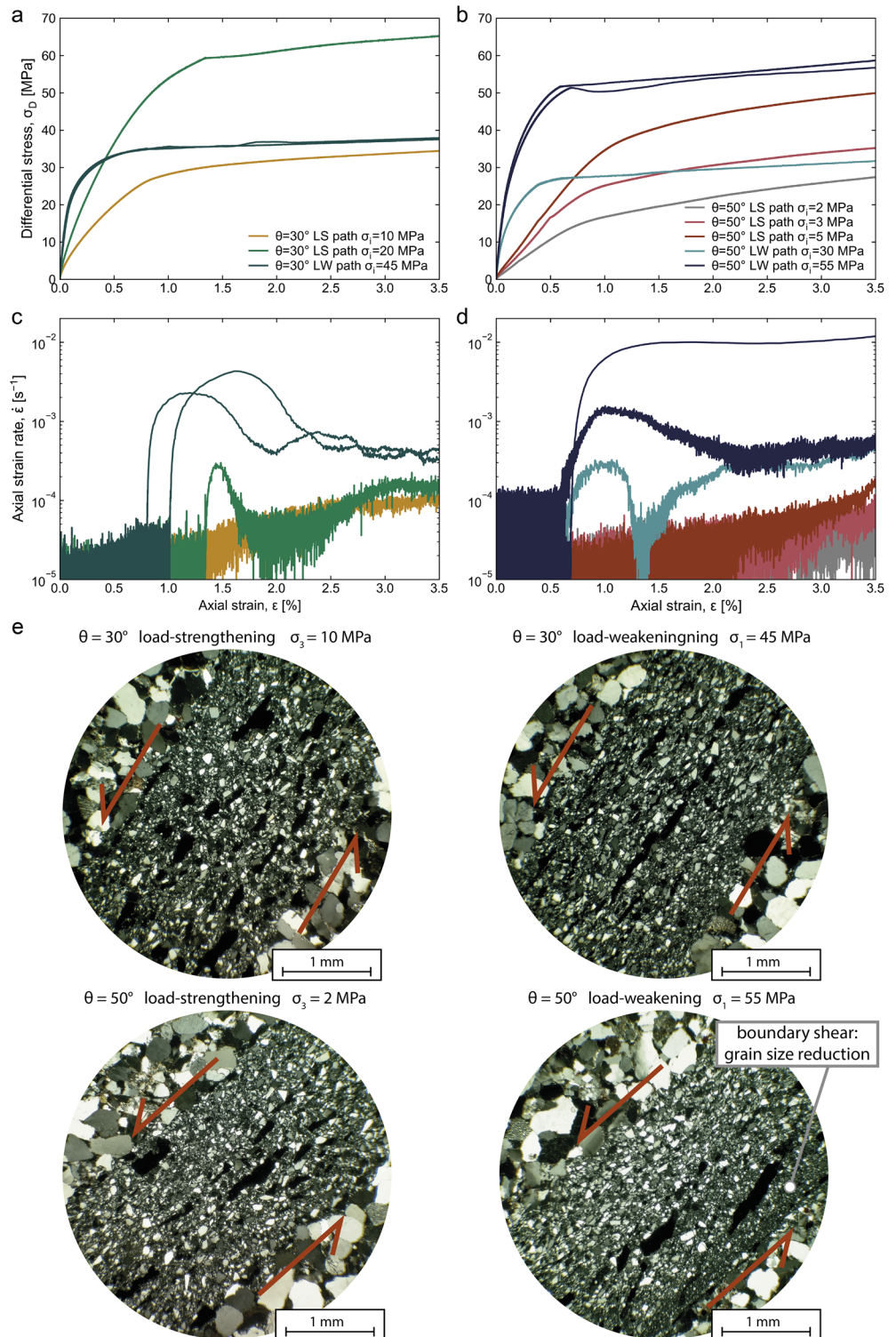
Figure 2. Mechanical results and microstructures from dry experiments: σ_D versus ε evolution for $\theta = 30°$ (a) and $\theta = 50°$ (b), $\dot{\varepsilon}$ versus ε evolution for $\theta = 30°$ (c) and $\theta = 50°$ (d). LWP results in stiffer behavior, whereas LSP results in more compliant behavior. Reactivation following LWPs results in an abrupt acceleration of $\dot{\varepsilon}$, whereas under LSPs $\dot{\varepsilon}$ smoothly accelerates. (e) Optical microscopy images of faults reactivated at the same σ_N under different conditions ($\theta = 30°$ vs. $\theta = 50°$ and LWP vs. LSP). Cataclastic flow is the main deformation process. The only exception is the fault at $\theta = 50°$ under LWP, where incipient localization occurs. LSP, load-strengthening path; LWP, load-weakening path.

the onset of a constant-rate strain-hardening in σ_D curve, which corresponds to the onset of a constant apparent steady-state friction $\mu_{SS} = \tau_{SS}/\sigma_N$ (Figure S1). Faults that underwent LWPs appear stiffer and achieve the steady-state at lower axial strain, $\varepsilon \approx 0.5\%$. Differently, faults that underwent LSPs appear more compliant and achieve the steady-state at $\varepsilon > 1.0\%$. Comparing σ_D evolution with $\dot{\varepsilon}$ evolution during LWPs Figures (2c and 2d), it is clear that during the non-linear increase in σ_D the fault creeps, resulting in $\dot{\varepsilon}$ the order of 10^{-5} s^{-1} until reactivation occurs. Once the σ_D for reactivation is achieved, the fault slip rate suddenly accelerates to $\dot{\varepsilon}$ of the order of 10^{-2} s^{-1}. In contrast, during LSPs, the fault creeps during the non-linear increase in σ_D at $\dot{\varepsilon}$ the order of 10^{-5} $s^{-1,}$ and when the σ_D for reactivation is approached its slip rate slowly and continuously accelerates. It should be mentioned that part of the measured axial displacement is due to the elastic deformation of the Rothbach sandstone, but we assume it to be negligible if compared to the inelastic deformation of the gouge (Figure S2). Moreover, since the experiments are conducted in load-control mode, the experimental procedure does not allow for stress drops when the experimental faults reactivate, and the reactivation is indicated by the acceleration of the slip rate.

The orientation of the fault to σ'_1 does not influence how reactivation occurs (abrupt vs. smooth fault slip rate acceleration), which is mainly controlled by the loading path as described above (Figure 2). However, μ_{SS} is slightly lower for misoriented than for well-oriented faults (Figure S1), that is, $\mu_{SS} = 0.63–0.75$ for $\theta = 50°$ and $\mu_{SS} = 0.74–0.84$ for $\theta = 30°$, as previously observed (Giorgetti et al., 2019; Savage et al., 1996).

Microstructures of post-mortem samples reactivated at same σ_N under different conditions ($\theta = 30°$ vs. $\theta = 50°$ and LWP vs. LSP) show that the deformation is distributed within the gouge layer and occurs via cataclastic flow. Only the experiment conducted at $\theta = 50°$ under LWP shows evidence of incipient localization and grain comminution at the boundary between the host rock and the gouge layer.

3.2. Water-Saturated Experiments

Figure 3 reports the mechanical results from water-saturated experiments. σ_D and $\dot{\varepsilon}$ evolutions are consistent with the observations collected from dry experiments. Additionally, water-saturated experiments give us a better insight into the behavior of faults under different loading paths through the evaluation of the volumetric strain.

A comparison of volumetric strain, σ_D, and $\dot{\varepsilon}$ evolutions with ε reveals that fault gouges experiencing LSPs undergo *compaction* until the steady-state σ_D is attained. During the steady-state, while the fault shears slowly ($\dot{\varepsilon} \approx 10^{-4}$ s^{-1}), the volume of the sample is also steady. Oppositely, an LWP results in *dilation* of the fault gouge during σ_D increase. Specifically, well-oriented faults attain a steady-state in volume coincident with the steady-state in σ_D and $\dot{\varepsilon}$, whereas misoriented faults show a higher amount of dilation that rapidly increases just before reactivation. After reactivation, misoriented faults show both dilation and compaction. However, once the fault slip rate abruptly accelerates, undrained conditions could locally develop within the gouge, and thus the evolution of the volumetric strain could be no more accurate.

Consistently with dry experiments and previous studies (Giorgetti et al., 2019; Savage et al., 1996), μ_{SS} is slightly lower for misoriented than for well-oriented faults (Figure S1), that is, $\mu_{SS} = 0.70–0.80$ for $\theta = 50°$ and $\mu_{SS} = 0.81–0.93$ for $\theta = 30°$. For load-weakening experiments, we considered only the apparent friction at which the slip rate abruptly starts to accelerate, in order not to consider data affected by possible local fluid overpressure.

4. Discussion

Figure 4 summarizes the results in τ versus σ_N planes. Under LSP, the deformation rate starts to slowly accelerate at τ well below the steady-state stress values (i.e., steady-state σ_D in Figures 2 and 3), especially for misoriented faults (e.g., inset in Figure 4b). In this latter case, the stress path is characterized by a flatter slope in τ versus σ_N plane (Figure 1b; Equation 2), resulting in τ that approaches the reactivation criterion even when σ_N and σ_D are still far from the values predicted for reactivation (Equation 1). The only exception consists of the experiment conducted at $\sigma_3 = 20$ MPa under dry conditions. Conversely, under LWPs, the deformation rate abruptly accelerates only when the stresses for reactivation are achieved (i.e., steady-state σ_D in Figures 2 and 3), with the only exception of the experiment conducted at $\sigma'_1 \approx 19$ MPa
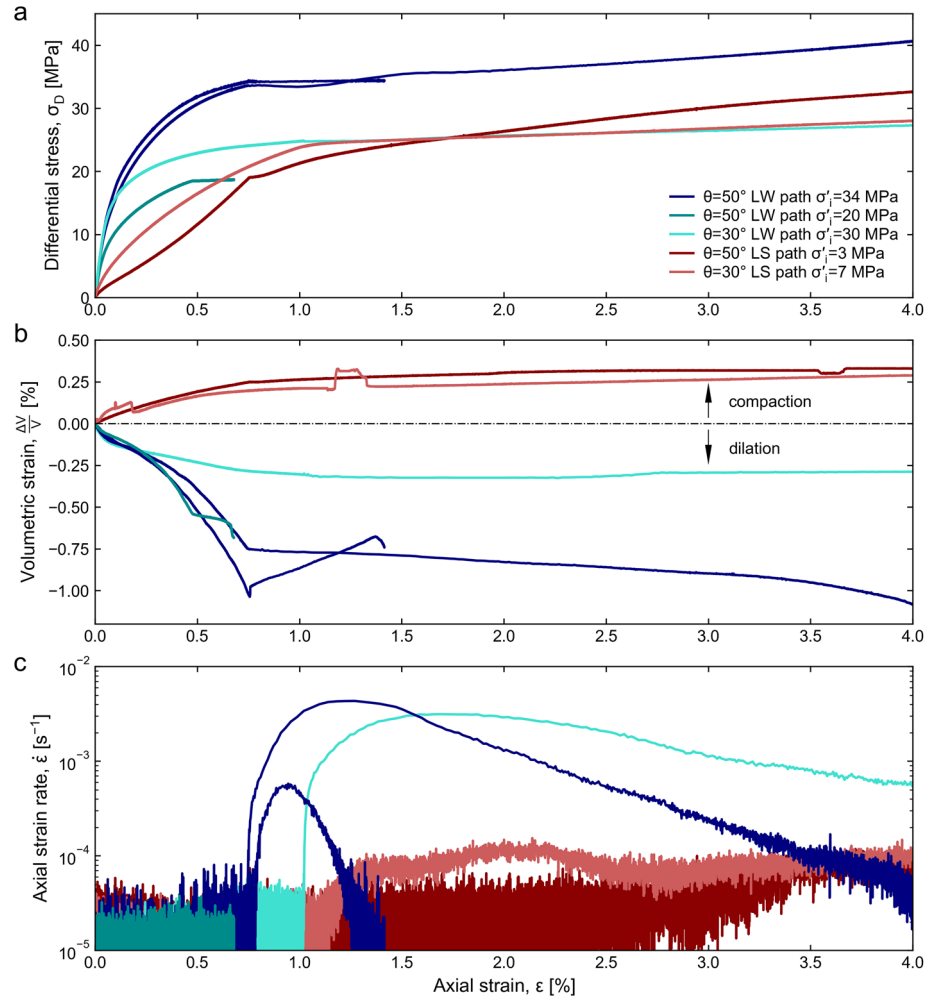
Figure 3. Mechanical results from water-saturated experiments: (a) σ_D versus ε for both $\theta = 30°$ and $\theta = 50°$, (b) volumetric strain versus ε for both $\theta = 30°$ and $\theta = 50°$, and (c) $\dot{\varepsilon}$ versus ε for both $\theta = 30°$ and $\theta = 50°$. The results are consistent with dry experiments results. The volumetric strain evolution shows that LWP results in dilation before reactivation, whereas LSP in compaction. LSP, load-strengthening path; LWP, load-weakening path.

under water-saturated conditions. Water-saturated and room-dry experiments show the same behavior and reactivation at comparable friction values ($\mu_{SS} \approx 0.63$–0.93). Therefore, we assume that the underlying mechanics is the same.

In terms of seismic behavior, we interpret the observed abrupt acceleration of the fault slip rate as the potential to nucleate earthquakes and the smooth acceleration of the fault slip rate has the potential to creep stably.

The observed mechanical behavior suggests that, even though reactivation occurs at comparable σ_N, faults undergoing LWP could slip seismically. In contrast, faults undergoing LSP could slip aseismically. To understand this contrasting behavior, we investigated the interplay between the elastic properties of the fault gouge and the surrounding loading system during the hydrostatic loading preceding the differential loading.

Once the σ_D for reactivation is achieved, the slip mode, that is, via stable versus unstable sliding, depends on the elastic interactions between the fault and the loading system (e.g., Rice, 1983). Conditions for instability are matched when the decrease of fault frictional strength with displacement, that is, the unloading stiffness of the fault $-k_f$, exceeds the unloading stiffness of the surrounding $-k_s$ (e.g., Kanamori & Brodsky, 2004; Rice, 1983): $k_f > k_s$.
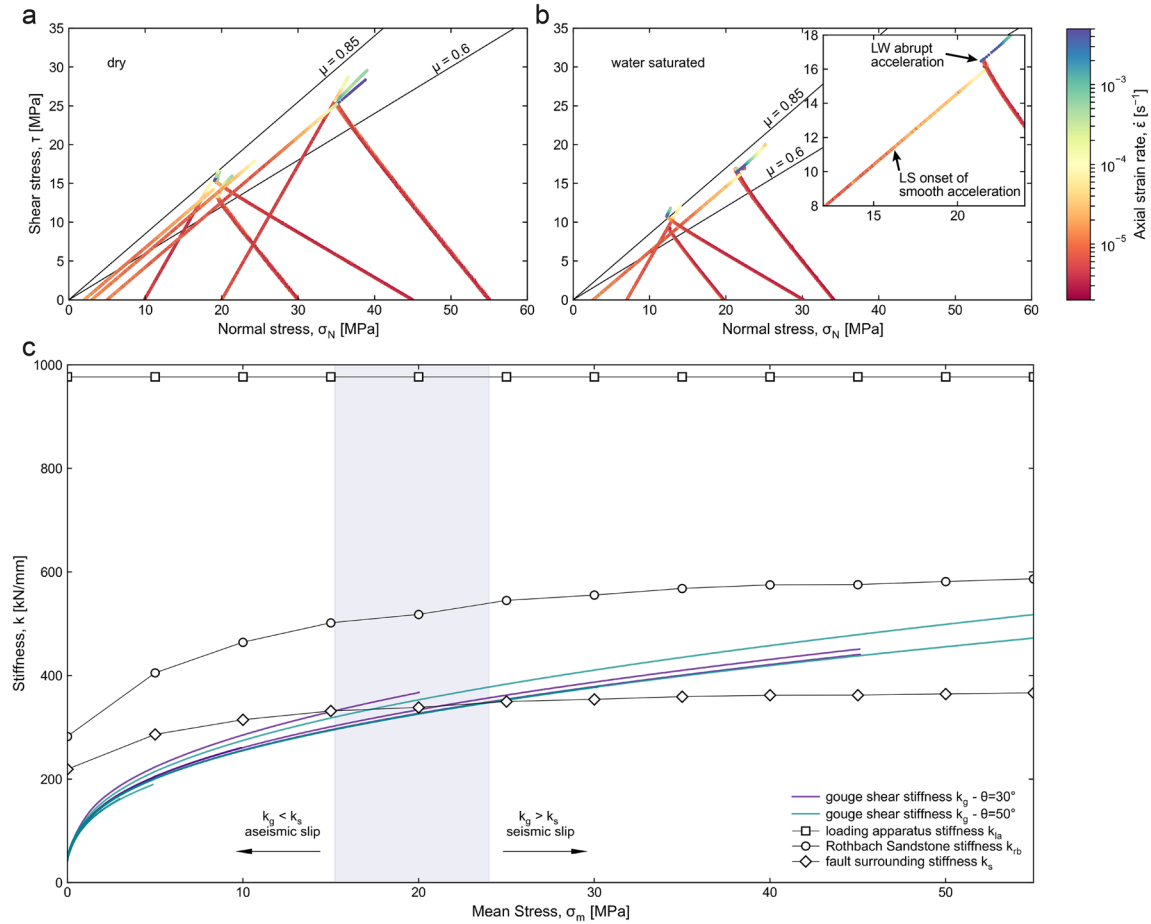
Figure 4. Mechanical results under dry (a) and water-saturated (b) conditions summarized in τ versus σ_N planes. Byerlee friction coefficients ($0.6 < \mu < 0.85$; Byerlee, 1978) are reported as a reference. (c) Interplay between the elastic properties of gouge (k_g) and fault surrounding (apparatus and sandstone) (k_s). At $\sigma_m < 15$–24 MPa, $k_g < k_{rb}$. At $\sigma_m > 15$–24 MPa, $k_g > k_{rb}$. Gouge that underwent $\sigma_m > 15$–24 MPa is more prone to slip seismically.

To characterize the stiffness of the surrounding k_s (Figure 4c), we combined the stiffness of the loading apparatus $k_{la} = 977$ kN/mm and the stiffness of the Rothbach sandstone k_{rb} (Figure 4c). To evaluate k_{rb}, we experimentally measured the travel time of ultrasonic waves through an intact sample of Rothbach sandstone at different hydrostatic stress (5–55 MPa) under dry conditions (Text S1; Figure S3a).

Then, to estimate the stiffness of the gouge layer k_g, we first inferred the evolution of the shear modulus of the fault gouge G_g from the change in porosity estimated during the hydrostatic pressure increase under dry conditions. To this end, a gouge layer can be approximated as a layer of packed spheres, and its shear modulus G_g can be evaluated as a function of the hydrostatic pressure σ_m depending on porosity ϕ as follows (Walton, 1987):

$$G_g = \frac{3}{5}\sqrt[3]{\frac{C^2\left(1-\varphi\right)^2 G^2}{18\pi^2\left(1-\nu\right)^2}}\sigma_m \tag{4}$$

where $G = 44$ GPa and $\nu = 0.07$ are the shear modulus and the Poisson's ratio of the solid quartz spheres (e.g., Mavko et al., 2020), and $C = 3$ is the coordination number (e.g., Dorostkar et al., 2018; Wang et al., 2019). The change in porosity during the hydrostatic loading is assumed to be homogeneous and equal to $\Delta V/V = 3\varepsilon$, and ε is assumed to be mainly accommodated by gouge compaction. The assumption of homogeneous porosity reduction is supported by microstructural observations (Figure 2e). The starting porosity of the gouge is ~45%, evaluated knowing the initial volume and weight of the gouge layer. It is noteworthy that we could not directly retrieve porosity changes in water-saturated experiments during the hydrostatic loading stage

due to water loss during sample saturation. However, the reliability of this model is further supported by the measured travel time of ultrasonic waves through a saw-cut sample filled with quartz gouge at different hydrostatic stress (Figure S4).

Consequently, the stiffness of the gouge layer k_g can be evaluated knowing the shear modulus and the geometry of the gouge layer as follow:

$$k_g = \frac{G_g \frac{r^2}{\sin \theta}}{h_g} \tag{5}$$

where r is the radius of the saw-cut sample ($\sim$36 mm) and h_g is the height of the gouge layer.

Figure 4c reports the resulting interplay between the stiffness of the surrounding loading system and the shear stiffness of the fault gouge with increasing hydrostatic pressure. There is a critical value of mean stress σ_m ($\approx$15–24 MPa) for higher values of which the fault gouge becomes stiffer than the surrounding medium. In our experiments, the hydrostatic pressure achieved during the hydrostatic loading stage affects the porosity of the gouge irreversibly and thus controls its stiffness (Equations 4 and 5) and the interaction with the elastic surrounding. Consistently, this critical value of σ_m separates seismic to aseismic behavior. Thus, faults that underwent LWP experienced starting hydrostatic pressure higher than the critical value (Figure 4 and Table S1), resulting in higher compaction and stiffer fault zone and enhancing unstable slip behavior. The two observed exceptions (LWP at $\sigma'_1 \approx 19$ MPa and LSP at $\sigma_3 = \sigma'_3 = 20$ MPa) further support our interpretation. It is worth noticing that, during the differential loading stage, σ_m evolves further, resulting in additional compaction under LSP and dilation under LWP (Figure 3b). As also shown by previous experiments under LSPs (Giorgetti et al., 2019), shear-enhanced compaction occurs in the gouge before the τ for reactivation and the steady-state are achieved. Therefore, k_g evolves also during the differential loading stage preceding fault reactivation. However, to quantify it further investigations are required.

5. Implications for Natural Faults

In general, the rise in τ on natural faults is associated with the change of σ_N across the fault (Sibson, 1992). Tectonic loading can be simplified as LWP for normal faults, due to the decrease of σ'_3 in extensional settings, and LSP for reverse faults, due to the increase of σ'_1 in compressional settings (Sibson, 1993). LWP is not exclusively characterizing normal faults, but it can characterize any kind of fault that, for a combination of tectonic loading and pore fluid pressure build-up, experiences a reduction in σ_N while τ increases. Exhumation and high erosional rates also affect the loading path of faults, reducing the lithostatic pressure. Natural and anthropogenic changes in fluid pressure modify σ'_N, thus imposing LWPs. In enhanced geothermal systems, stress-preconditioning designed for mitigating the seismic risk (e.g., Fryer et al., 2020) also affects the loading path. Additionally, if a fault nucleates an earthquake, the fault surrounding consequently experiences a change in both τ and σ_N (e.g., Rice & Gu, 1983). Therefore, the influence of the loading path in the mechanics of fault reactivation must be appropriately constrained (e.g., Hirakawa & Ma, 2016), especially in mature faults characterized by the presence of a thick fault zone (e.g., Ben-Zion & Sammis, 2003; Caine et al., 1996; Faulkner et al., 2011; Shipton et al., 2006). In fact, incohesive fault rocks have a high potential for dilation and compaction under conditions of evolving the stress state. Although fault rocks often regain cohesion during the interseismic periods at seismogenic depth (5–15 km), incohesive fault rocks are commonly observed at shallow depth (<5 km) where they can host earthquakes induced by human underground activities (e.g., quarry extraction, Ritz et al., 2020; deep gold mines; Mngadi et al., 2021) and tectonic earthquakes (e.g., Champenois et al., 2017; Kyriakopoulos, 2013; Thouvenot et al., 1998).

Our study shows that critically stressed, gouge-bearing faults clamped by a given σ_N may both slip seismically or aseismically depending on their loading path and their stress history. Particularly, we infer that faults undergoing LWPs, that is, faults that experienced higher σ_N than the σ_N for reactivation, are more prone to slip seismically than faults undergoing LSPs. However, it is worth mentioning that seismic versus aseismic slip is ultimately controlled by the interplay between the unloading stiffness of the fault and the elastic properties of the surrounding (e.g., Goodman & Sundaram, 1978; Kanamori & Brodsky, 2004).

Frictional instability of faults is often described within the framework of the rate- and state-dependent friction (e.g., Dieterich, 1972, p. 1979; Ruina, 1983). The rate-and-state approach is usually adopted in the laboratory to retrieve empirical parameters that are used as inputs for numerical modeling studies (e.g., McClure & Horne, 2011; Noda et al., 2017). Recent experimental works on gouge have shown that the transition between stable and unstable slip can be crossed by the only change in σ_N (e.g., Leeman et al., 2016; Scuderi et al., 2016), in agreement with rate- and state-dependent friction laws. However, this theoretical framework considers only the σ_N at which the fault slips and not its σ_N history. Based on our experimental results, we suggest that for gouge-bearing faults the stress history and the loading path cannot be neglected when assessing fault slip stability. Thus, models evaluating fault seismic potential using a rate-and-state approach and considering only the σ_N at reactivation could be misleading. Recently, microphysical models have been developed for gouge frictional stability, as an alternative to the rate-and-state approach (Chen & Spiers, 2016; van den Ende et al., 2020; Niemeijer & Spiers, 2007). These models relate fault slip to porosity changes, supporting our interpretation. The stress history of a fault controls how the porosity, and thus the stiffness, of the gouge, evolves before reactivation.

Finally, our study has also implications for fluid circulation. The observed contrasting volumetric behavior under LSP versus LWP would favor a contrasting hydrological behavior. Incohesive normal fault zones and fault zones that undergo a decrease in σ_N would experience an enhanced permeability before reactivation, whereas incohesive reverse fault zones and fault zone that undergo a decrease in σ_N would experience a hindered permeability before reactivation. However, the role of fluid pressure changes in different loading paths, fundamental both in natural and induced seismicity, needs to be further investigated.

6. Conclusions

We investigated the role of the loading path on gouge-bearing fault reactivation, inducing shear in gouge under triaxial saw-cut configuration. We document for the first time a contrasting hydro-mechanical behavior under LWP versus LSP. Particularly, our data show *dilation* before reactivation for LWPs and *compaction* before reactivation for LSPs. Moreover, given the same σ_N for reactivation, faults experiencing LWPs are more prone to slip seismically than faults experiencing LSPs. Overall, these observations are valid for both well-oriented and misoriented faults. We interpret this contrasting behavior (dilation vs. compaction; seismic vs. aseismic) as a consequence of the fault stress history. Specifically, an LWP results in higher mean stress that the fault zone undergoes before reactivation, leading to denser and stiffer gouge, more prone to nucleate earthquakes, than an LSP. Our findings have strong implications for shallow portions of gouge-bearing natural faults, suggesting that stress history and loading-path cannot be neglected when evaluating fault slip stability.

Data Availability Statement

The data that support the findings of this study are openly available in Mendeley Data at http://dx.doi.org/10.17632/3rhm75f534.1.

References

Agosta, F., & Aydin, A. (2006). Architecture and deformation mechanism of a basin-bounding normal fault in Mesozoic platform carbonates, central Italy. *Journal of Structural Geology*, *28*(8), 1445–1467. https://doi.org/10.1016/j.jsg.2006.04.006

Anderson, E. M. (1905). The dynamics of faulting. *Transactions of the Edinburgh Geological Society*, *8*, 387–402. https://doi.org/10.1144/transed.8.3.387

Ben-Zion, Y., & Sammis, C. G. (2003). Characterization of fault zones. *Pure and Applied Geophysics*, *160*(3–4), 677–715. https://doi.org/10.1007/PL00012554

Bésuelle, P., Baud, P., & Wong, T. (2003). Failure mode and spatial distribution of damage in Rothbach sandstone in the brittle-ductile transition. *Pure and Applied Geophysics*, *160*, 851–868. https://doi.org/10.1007/PL00012569

Bolognesi, F., & Bistacchi, A. (2016). Weakness and mechanical anisotropy of phyllosilicate-rich cataclasites developed after mylonites of a low-angle normal fault (Simplon Line, Western Alps). *Journal of Structural Geology*, *83*, 1–12. https://doi.org/10.1016/j.jsg.2015.11.009

Byerlee, J. (1978). Friction of rocks. *Pure and Applied Geophysics*, *116*, 615–626. https://doi.org/10.1007/BF00876528

Caine, J. S., Evans, J. P., & Forster, C. B. (1996). Fault zone architecture and permeability structure. *Geology*, *24*(11), 1025–1028. https://doi.org/10.1130/0091-7613(1996)024<1025:FZAAPS>2.3.CO;2

Champenois, J., Baize, S., Vallee, M., Jomard, H., Alvarado, A., Espin, P., et al. (2017). Evidences of surface rupture associated with a low-magnitude (Mw5.0) shallow earthquake in the Ecuadorian Andes. *Journal of Geophysical Research: Solid Earth*, *122*, 8446–8458. https://doi.org/10.1002/2017JB013928

Chen, J., & Spiers, C. J. (2016). Rate and state frictional and healing behavior of carbonate fault gouge explained using microphysical model. *Journal of Geophysical Research: Solid Earth*, *121*, 8642–8665. https://doi.org/10.1002/2016JB013470

Chester, F. M., & Logan, J. M. (1990). Frictional faulting in polycrystalline halite: Correlation of microstructure, mechanisms of slip, and constitutive behavior. In A. G. Duba, W. B. Durham, J. W. Handin, & H. F. Wang (Eds.), *The Brittle-Ductile transition in rocks* (pp. 49–65). https://doi.org/10.1029/GM056p0049

Collettini, C., & Trippetta, F. (2007). A slip tendency analysis to test mechanical and structural control on aftershock rupture planes. *Earth and Planetary Science Letters*, *255*(3–4), 402–413. https://doi.org/10.1016/j.epsl.2007.01.001

Copley, A. (2017). The strength of earthquake-generating faults. *Journal of the Geological Society*, *175*, 1–12. https://doi.org/10.1144/jgs2017-037

Dieterich, J. H. (1972). Time-dependent friction in rocks. *Journal of Geophysical Research*, *77*(20), 3690–3697. https://doi.org/10.1029/JB077i020p03690

Di Toro, G., Han, R., Hirose, T., De Paola, N., Nielsen, S., Mizoguchi, K., et al. (2011). Fault lubrication during earthquakes. *Nature*, *471*, 494–498. https://doi.org/10.1038/nature09838

Dorostkar, O, Guyer, R. A., Johnson, P. A., Marone, C., & Carmeliet, J. (2018). Cohesion-induced stabilization in stick-slip dynamics of weakly wet, sheared granular fault gouge. *Journal of Geophysical Research: Solid Earth*, *123*, 2115–2126. https://doi.org/10.1002/2017jb015171

Faulkner, D. R., Mitchell, T. M., Jensen, E., & Cembrano, J. (2011). Scaling of fault damage zones with displacement and the implications for fault growth processes. *Journal of Geophysical Research*, *116*, B05403. https://doi.org/10.1029/2010JB007788

Ferraro, F., Agosta, F., Prasad, M., Vinciguerra, S., Violay, M., & Giorgioni, M. (2020). Pore space properties in carbonate fault rocks of peninsular Italy. *Journal of Structural Geology*, *130*, 103913. https://doi.org/10.1016/j.jsg.2019.103913

French, M. E., Zhu, W., & Banker, J. (2016). Fault slip controlled by stress path and fluid pressurization rate. *Geophysical Research Letters*, *43*, 4330–4339. https://doi.org/10.1002/2016GL068893

Fryer, B., Siddiqi, G., & Laloui, L. (2020). Injection-induced seismicity: Strategies for reducing risk using high stress path reservoirs and temperature-induced stress preconditioning. *Geophysical Journal International*, *220*(2), 1436–1446. https://doi.org/10.1093/gji/ggz490

Gan, Q., & Elsworth, D. (2014). Analysis of fluid injection-induced fault reactivation and seismic slip in geothermal reservoirs. *Journal of Geophysical Research: Solid Earth*, *119*, 3340–3353. https://doi.org/10.1002/2013JB010679

Giorgetti, C., Tesei, T., Scuderi, M. M., & Collettini, C. (2019). Experimental insights into fault reactivation in gouge-filled fault zones. *Journal of Geophysical Research: Solid Earth*, *124*, 4189–4204. https://doi.org/10.1029/2018JB016813

Goodman, R. E., & Sundaram, P. N. (1978). Fault and system stiffnesses and stick-slip phenomena. *Pure and Applied Geophysics*, *116*(1978), 873–887. https://doi.org/10.1007/BF00876543

Harris, R. A., & Simpson, R. W. (1992). Changes in static stress on southern California faults after the 1992 Landers earthquake. *Nature*, *360*(6401), 251–254. https://doi.org/10.1038/360251a0

Hirakawa, E., & Ma, S. (2016). Dynamic fault weakening and strengthening by gouge compaction and dilatancy in a fluid-saturated fault zone. *Journal of Geophysical Research: Solid Earth*, *121*, 5988–6008. https://doi.org/10.1002/2015JB012509

Jacquey, A. B., Cacace, M., Blöcher, G., & Scheck-Wenderoth, M. (2015). Numerical investigation of thermoelastic effects on fault slip tendency during injection and production of geothermal fluids. *Energy Procedia*, *76*, 311–320. https://doi.org/10.1016/j.egypro.2015.07.868

Jaeger, J. C. (1960). Shear Failure of Anistropic Rocks. *Geological Magazine*, *97*, 65–72. https://doi.org/10.1017/S0016756800061100

Kanamori, H., & Brodsky, E. E. (2004). The physics of earthquakes. *Reports on Progress in Physics*, *67*, 1429–1496. https://doi.org/10.1088/0034-4885/67/8/R03

Kyriakopoulos, C., Chini, M., Bignami, C., Stramondo, S., Ganas, A., Kolligri, M., & Moshou, A. (2013). Monthly migration of a tectonic seismic swarm detected by DInSAR: Southwest Peloponnese, Greece. *Geophysical Journal International*, *194*, 1302–1309. https://doi.org/10.1093/gji/ggt196

Leclère, H., & Fabbri, O. (2013). A new three-dimensional method of fault reactivation analysis. *Journal of Structural Geology*, *48*, 153–161. https://doi.org/10.1002/2014TC00360010.1016/j.jsg.2012.11.004

Leeman, J. R., Saffer, D. M., Scuderi, M. M., & Marone, C. (2016). Laboratory observations of slow earthquakes and the spectrum of tectonic fault slip modes. *Nature Communications*, *7*, 11. https://doi.org/10.1038/ncomms11104

Lisle, R. J., & Srivastava, D. C. (2004). Test of the frictional reactivation theory for faults and validity of fault-slip analysis. *Geology*, *32*(7), 569–572. https://doi.org/10.1130/G20408.1

Marone, C. (1998). Laboratory-derived friction laws and their application to seismic faulting. *Annual Review of Earth and Planetary Sciences*, *26*(1), 643–696. https://doi.org/10.1146/annurev.earth.26.1.643

Mavko, G., Mukerji, T., & Dvorkin, J. (2020). *The rock physics handbook*. Cambridge university press. https://doi.org/10.1017/9781108333016

McClure, M. W., & Horne, R. N. (2011). Investigation of injection-induced seismicity using a coupled fluid flow and rate/state friction model. *Geophysics*, *76*, WC181–WC198. https://doi.org/10.1190/geo2011-0064.1

Mngadi, S. B., Tsutsumi, A., Onoe, Y., Manzi, M. S. D., Durrheim, R. J., Yabe, Y., et al. (2021). The effect of a gouge layer on rupture propagation along brittle shear fractures in deep and high-stress mines. *International Journal of Rock Mechanics and Mining Sciences*, *137*, 104454. https://doi.org/10.1016/j.ijrmms.2020.104454

Moeck, I., Kwiatek, G., & Zimmermann, G. (2009). Slip tendency analysis, fault reactivation potential and induced seismicity in a deep geothermal reservoir. *Journal of Structural Geology*, *31*(10), 1174–1182. https://doi.org/10.1016/j.jsg.2009.06.012

Morris, A., Ferrill, D. A., & Brent Henderson, D. B. (1996). Slip-tendency analysis and fault reactivation. *Geology*, *24*(3), 275–278. https://doi.org/10.1130/0091-7613(1996)024<0275:STAAFR>2.3.CO;2

Niemeijer, A. R., & Spiers, C. J. (2007). A microphysical model for strong velocity weakening in phyllosilicate-bearing fault gouges. *Journal of Geophysical Research*, *112*, B10405. https://doi.org/10.1029/2007JB005008

Noël, C., Passelègue, F. X., Giorgetti, C., & Violay, M. (2019). Fault reactivation during fluid pressure oscillations: Transition from stable to unstable slip. *Journal of Geophysical Research. Solid Earth*, *124*, 10940–10953. https://doi.org/10.1029/2019JB018517

Noda, H., Sawai, M., & Shibazaki, B. (2017). Earthquake sequence simulations with measured properties for JFAST core samples. *Philosophical Transactions of the Royal Society of A*, *375*, 20160003. https://doi.org/10.1098/rsta.2016.0003

Passelègue, F. X., Almakari, M., Dublanchet, P., Barras, F., Fortin, J., & Violay, M. (2020). Initial effective stress controls the nature of earthquakes. *Nature Communications*, *11*, 5132. https://doi.org/10.1038/s41467-020-18937-0

Passelègue, F. X., Brantut, N., & Mitchell, T. M. (2018). Fault reactivation by fluid injection: Controls from stress state and injection rate. *Geophysical Research Letters*, *45*, 12837–12846. https://doi.org/10.1029/2018GL080470

Petruccelli, A., Schorlemmer, D., Tormann, T., Rinaldi, A. P., Wiemer, S., Gasperini, P., & Vannucci, G. (2019). The influence of faulting style on the size-distribution of global earthquakes. *Earth and Planetary Science Letters*, *527*, 115791. https://doi.org/10.1016/j.epsl.2019.115791

Rice, J. R. (1983). Constitutive relations for fault slip and earthquake instabilities. *Pageoph*, *121*, 443–475. https://doi.org/10.1007/BF02590151

Rice, J. R., & Gu, J.-C. (1983). Earthquake aftereffects and triggered seismic phenomena. *Pure and Applied Geophysics*, *121*, 187–219. https://doi.org/10.1007/BF02590135

Ritz, J.-F., Baize, S., Ferry, M., Larroque, C., Audin, L., Delouis, B., & Mathot, E. (2020). Surface rupture and shallow fault reactivation during the 2019 Mw 4.9 Le Teil earthquake, France. *Communications Earth & Environment*, *1*, 10. https://doi.org/10.1038/s43247-020-0012-z

Ruina, A. (1983). Slip instability and state variable friction laws. *Journal of Geophysical Research*, *88*(B12), 10359–10370. https://doi.org/10.1029/JB088iB12p10359

Rutter, E., & Hackston, A. (2017). On the effective stress law for rock-on-rock frictional sliding, and fault slip triggered by means of fluid injection. *Philosophical Transactions of the Royal Society of A*, *375*, 20160001. https://doi.org/10.1098/rsta.2016.0001

Rutter, E. H., & Glover, C. T. (2012). The deformation of porous sandstones; are Byerlee friction and the critical state line equivalent? *Journal of Structural Geology*, *44*, 129–140. https://doi.org/10.1016/j.jsg.2012.08.014

Rutter, E. H., & Maddock, R. H. (1992). On the mechanical properties of synthetic kaolinite/quartz fault gouge. *Terra Nova*, *4*, 489–500. https://doi.org/10.1111/j.1365-3121.1992.tb00585.x

Savage, J. C., Lockner, D. A., & Byerlee, J. D. (1996). Failure in laboratory fault models in triaxial tests. *Journal of Geophysical Research*, *101*(B10), 22215–22224. https://doi.org/10.1029/96JB02094

Schofield, A. N., & Wroth, C. P. (1968). *Critical state soil mechanics*. McGraw-Hill.

Schorlemmer, D., Wiemer, S., & Wyss, M. (2005). Variations in earthquake-size distribution across different stress regimes. *Nature*, *437*, 539–542. https://doi.org/10.1038/nature04094

Scuderi, M. M., & Collettini, C. (2018). Fluid injection and the mechanics of frictional stability of shale-bearing faults. *Journal of Geophysical Research: Solid Earth*, *123*, 8364–8384. https://doi.org/10.1029/2018JB016084

Scuderi, M. M., Marone, C., Tinti, E., Di Stefano, G., & Collettini, C. (2016). Precursory changes in seismic velocity for the spectrum of earthquake failure modes. *Nature Geosciences*, *9*, 695–700. https://doi.org/10.1038/ngeo2775

Shipton, Z. K., Soden, A. M., Kirkpatrick, J. D., Bright, A. M., & Lunn, R. J. (2006). How thick is a fault? Fault displacement-thickness scaling revisited. In R. E. Abercombie, A. McGarr, H. Kanamori, & G. Di Toro (Eds.), *Earthquakes: Radiated energy and the physics of faulting* (pp. 193–198). https://doi.org/10.1029/170GM19

Sibson, R. H. (1985). A note on fault reactivation. *Journal of Structural Geology*, *7*(6), 751–754. https://doi.org/10.1016/0191-8141(85)90150-6

Sibson, R. H. (1992). Implications of fault-valve behavior for rupture nucleation and recurrence. *Tectonophysics*, *211*(1–4), 283–293. https://doi.org/10.1016/0040-1951(92)90065-E

Sibson, R. H. (1993). Load-strengthening versus load-weakening faulting. *Journal of Structural Geology*, *15*(2), 123–128. https://doi.org/10.1016/0191-8141(93)90090-W

Sumy, D. F., Cochran, E. S., Keranen, K. M., Wei, M., & Abers, G. A. (2014). Observations of static Coulomb stress triggering of the November 2011 M 5.7 Oklahoma earthquake sequence. *Journal of Geophysical Research: Solid Earth*, *119*, 1904–1923. https://doi.org/10.1002/2013JB010612

Thouvenot, F., Fréchet, J., Tapponnier, P., Thomas, J.-C., Le Brun, B., Ménard, G., et al. (1998). The ML5.3 Épagny (French Alps) earthquake of 1996 July 15: A long-awaited event on the Vuache fault. *Geophysical Journal International*, *135*, 876–892. https://doi.org/10.1046/j.1365-246X.1998.00662.x

van den Ende, M. P. A., Scuderi, M. M., Cappa, F., & Ampuero, J.-P. (2020). Extracting microphysical fault friction parameters from laboratory- and field injection experiments. *Solid Earth Discussion*. https://doi.org/10.5194/se-2020-118

Walton, K. (1987). The effective elastic moduli of a random packing of spheres. *Journal of the Mechanics and Physics of Solids*, *35*(2), 213–226. https://doi.org/10.1016/0022-5096(87)90036-6

Wang, C., Elsworth, D., & Fang, Y. (2019). Ensemble shear strength, stability, and permeability of mixed mineralogy fault gouge recovered from 3D granular models. *Journal of Geophysical Research: Solid Earth*, *124*, 425–441. https://doi.org/10.1029/2018JB016066

Williams, J. N., Fagereng, Å., Wedmore, L. N. J., Biggs, J., Mphepo, F., Dulanya, Z., et al. (2019). How do variably striking faults reactivate during rifting? Insights from southern Malawi. *Geochemistry, Geophysics, Geosystems*, *20*, 3588–3607. https://doi.org/10.1029/2019GC008219

Worum, G., van Wees, J.-D., Bada, G., van Balen, R. T., Cloetingh, S., & Pagnier, H. (2004). Slip tendency analysis as a tool to constrain fault reactivation: A numerical approach applied to three-dimensional fault models in the Roer Valley rift system (southeast Netherlands). *Journal of Geophysical Research*, *109*, B02401. https://doi.org/10.1029/2003JB002586

Reference From the Supporting Information

Louis, L., Baud, P., & Wong, T.-f. (2009). Microstructural inhomogeneity and mechanical anisotropy associated with bedding in Rothbach sandstone. *Pure and Applied Geophysics*, *166*, 1063–1087. https://doi.org/10.1007/s00024-009-0486-1